Slanted-pore photonic band-gap materials

Ovidiu Toader and Sajeev John
Department of Physics, University of Toronto, 60 St. George Street, Toronto, Ontario, Canada M5S 1A7
(Received 31 May 2004; revised manuscript received 14 October 2004; published 11 March 2005)

We present a detailed analysis of three-dimensional photonic band-gap materials consisting of lattices of slanted pores with $n=2$, 3, and 4 pores per unit cell. These slanted pores emanate from one or two masks consisting of a two-dimensional square or triangular lattice of holes placed on the top surface of the crystal. We also consider the case in which the top surface is "polished" at an angle after the first set of slanted pores is generated from the first mask. A second set of slanted pores is then generated from a second mask placed on the new angled surface. Using these architectures, we demonstrate photonic band gaps of up to 25% of the gap center frequency when the crystal is made from materials with a dielectric constant ratio of 11.9:1 (silicon with air pores). The proposed structures are amenable to microfabrication using established techniques such as x-ray lithography or two-photon direct writing in a polymer template, followed by inversion and replication of the template with polycrystalline silicon. They can also be microfabricated by direct plasma etching in single crystal semiconductors. An alternative fabrication protocol consists of photoelectrochemical etching of deep pores in a single crystal semiconductor followed by focused ion beam or reactive ion etching of the second lattice of directed pores.

DOI: 10.1103/PhysRevE.71.036605 PACS number(s): 42.70.Qs

I. INTRODUCTION

Since the introduction of the photonic band-gap (PBG) concept [1,2], there has been considerable interest in the design of materials that are amenable to large scale, low cost microfabrication, and which exhibit a large PBG. Slanted pore structures [3] are of particular interest because they can exhibit a significant PBG while at the same time being amenable to microfabrication by a variety of techniques such as x-ray lithography [4–11], two-photon direct writing [12–15], photoelectrochemical etching [16–18], ion beam etching [19–24], or a combination of the above. It is particularly interesting to develop architectures and fabrication protocols in which circuits of light [25] can be readily incorporated using the same methods. Such optical circuits would operate using the principle of light localization [26,27], rather than total internal reflection for guiding light, and would enable frequency selective control of spontaneous emission from nearby atoms and molecules [2,28–30]. The combination of these two properties enables the development of robust forms of integrated optics. Here, passive waveguiding of light can be combined with active microphotonic devices on an optical microchip. These possibilities have inspired a broad range of scientists and engineers to design and synthesize microstructures exhibiting a large photonic band gap. The identification of the diamond lattice [31] as a primary candidate for a large three-dimensional (3D) PBG has led to the design [32,33] and microfabrication [34–36] of woodpile-type structures. An alternative square spiral structure with a potentially larger 3D PBG [37,38] and amenable to lower cost synthesis [39,40] has been realized more recently [41]. Likewise, self-assembly methods have achieved very large scale face centered cubic (fcc) lattices with a high degree of perfection, but with a relatively small PBG [42,43]. On the other hand, low loss optical circuitry on a large scale, a PBG based microchip, operating at visible or near infrared wavelengths, may require manufacturing of structures with a precision of a few nanometers. This necessitates the consideration of architectures that are amenable to microfabrication using high resolution techniques such as x-ray lithography into a polymer template followed by inversion and replication with silicon [4]. For optoelectronic applications, it is also advantageous to develop PBG materials in which the dielectric backbone consists of a high quality single crystal semiconductor.

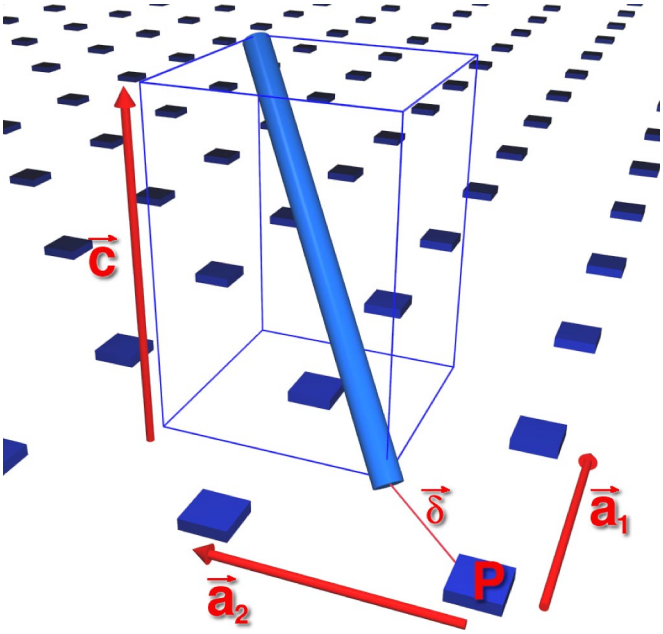

FIG. 1. (Color online) An example of a SP_1 structure. The square mask is characterized by unit vectors $\vec{a}_1=(a,0,0)$ and $\vec{a}_2=(0,a,0)$. $\vec{c}=(0,0,c)$ is a vector perpendicular to the mask plane. The pore axis associated with mask point P starts at position $\vec{\delta}=0.5\vec{a}_1+0.5\vec{a}_2$ relative to P and ends at $\vec{\delta}+1\vec{a}_1+1\vec{a}_2+\vec{c}$. This particular structure belongs to family $S/[1,1]^{(0.5,0.5)}$.

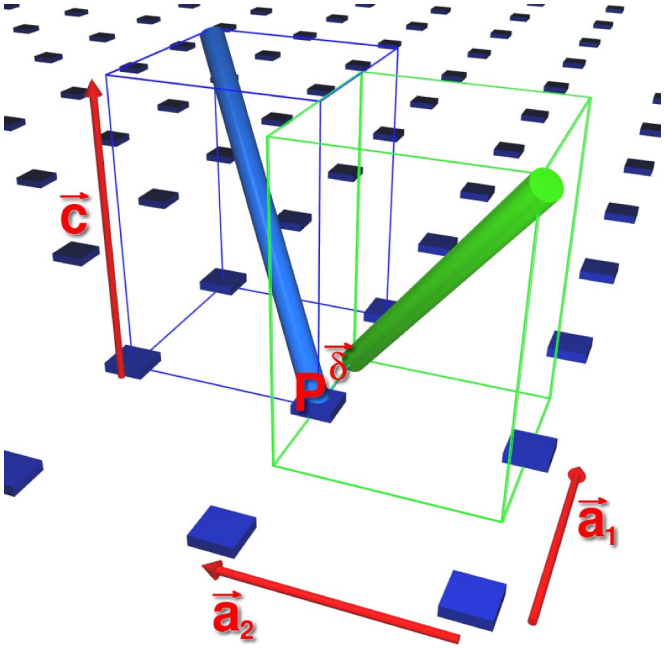

FIG. 2. (Color online) An example of a SP_2 structure based on a square mask $S/[1,1]\oplus[-1,-1]^{(0.5,0)}$. The two pore axes associated with the mask point P are illustrated. The intersection between the second pore axis and the mask plane is shifted by $\vec{\delta}=0.5\vec{a}_1+0\vec{a}_2$ relative to P. We make use of the convention $[1,1]\equiv[1,1]^{(0,0)}$.

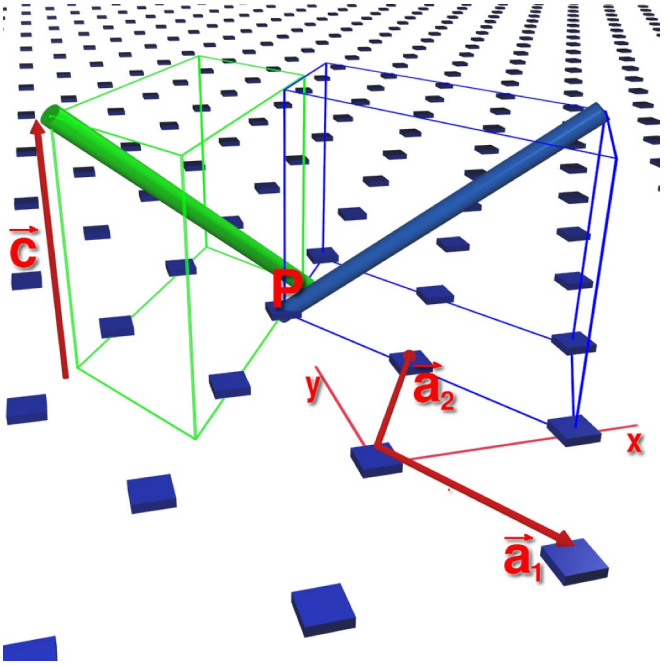

FIG. 3. (Color online) An example of a SP_2 structure based on a triangular mask $T/[2,1]\oplus[-1,-2]^{(0,0.5)}$. The primitive unit vectors of the triangular mask are $\vec{a}_{1,2}=((1/2)a, \mp(\sqrt{3}/2)a, 0)$, where a is the lattice constant of the mask.

Early studies suggested the possibility of achieving a moderate size 3D PBG using a lattice of crisscrossing pores [44]. The "Yablonovite" structure consists of three pores oriented along the three primitive lattice vectors of the fcc lattice and emanating from a triangular mask on the sample surface. In principle, it exhibits a 17% PBG when made from optimized air cylinders in a silicon background of dielectric constant $\varepsilon=11.9$. While this structure has been fabricated for microwave applications, the corresponding semiconductor material with sub-micrometer diameter pores has been difficult to achieve using reactive ion etching methods [19,20]. It is both difficult to drill directly into the semiconductor to more than a few micrometers depth and nearly impossible to maintain sharply defined cylinder shapes near the crossing points of the pores. Focused ion beam etching has recently been introduced in order to obtain deeper etches, but a complete PBG remains to be demonstrated. A closely related structure, referred to as "Kielovite" [45], has been synthesized on a very large scale using photoelectrochemical etching [16,18] in silicon and various III-V semiconductors. In silicon, this structure involves a triangular lattice of etch pits on the (1,1,1) crystallographic surface. Photoelectrochemical etching then leads to a set of three pores (symmetrically placed on a 29.5° cone with respect to the surface normal) emanating from each etch pit. This entails a tetragonal distortion of the Yablonovite, which requires a 35.3° cone. The PBG of the Kielovite is only 8% of the gap center frequency when optimized [46]. Moreover, the photoelectrochemical etching process requires doping of the semiconductor, resulting in sometimes undesirable, free charge carriers in the resulting PBG material.

Recently, another approach to 3D photonic crystal synthesis based on ultraviolet holography in a polymer template [47] has been proposed. In this method, the interference pattern of four laser beams is used to expose a polymer photoresist. After a "baking" and "developing" process the over- or underexposed regions are removed, leaving behind a replica of the laser isointensity surfaces. A variety of PBG architectures have recently been identified [48] for this type of interference lithography. A large PBG occurs provided the polymer template is replicated with a high index of refraction material, such as silicon.

Up to now the use of x-ray lithography to create slanted-pore (SP) photonic crystals has been restricted to Yablonovite structures in low refractive index polymers (photoresists) and 10-μm, scale pores [5–9]. Using this method, nanometer scale resolution is possible. In order to achieve a photonic band gap, a double inversion of the polymer template is required. In the LIGA (Lithographie, Galvanoformung und Abformung) technique [4,10], the pores in the polymer template are infiltrated with a metal and the polymer is subsequently removed, yielding an "inverse" structure. This metallic photonic crystal can, in principle, be used as a second template for chemical vapor deposition of silicon throughout its void regions. As in the case of inverse opals [42], selective etching of the metal template yields the desired "direct" structure (replica of the original polymer template), now consisting of air pores in a silicon background. The reduction in feature size, to create a PBG centered at a wavelength of 1.5 μm, using LIGA, requires the careful development of high quality masks which can stop the x rays from etching the polymer template in regions other than the desired pores. The polymer template can also be exposed using two-photon absorption based direct writing. This technique does not provide the high resolution of x-ray lithogra-

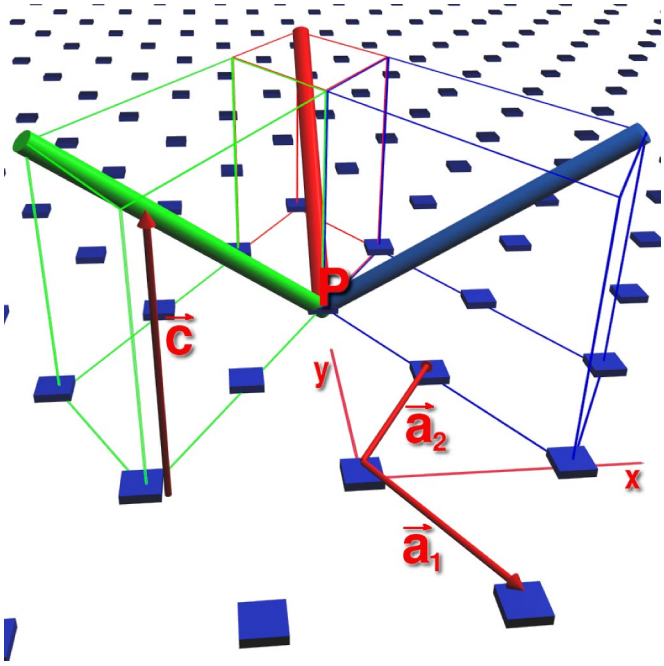

FIG. 4. (Color online) An example of a SP_3 structure based on a triangular mask $T/[2,1]\oplus[-1,1]\oplus[-1,-2]$. The primitive unit vectors of the triangular mask are $\vec{a}_{1,2}=((1/2)a, \mp(\sqrt{3}/2)a, 0)$, where a is the lattice constant of the mask. When $c=\sqrt{6}a$ the structure is identical with Yablonovite [44].

phy. However, the direct writing technique may be useful for creating waveguide circuits and microcavity defects, once the underlying 3D PBG crystal has been imprinted on the polymer photoresist.

In this paper we introduce a set of slanted-pore (SP_n) photonic crystal architectures consisting of $n=2,3,4$ pores per unit cell. In addition to having gaps as large as 25% of the gap center frequency, some of the structures involve fewer pore crossings than Yablonovite and therefore are less prone to disorder-induced degradation of the photonic band gap. A special nomenclature is introduced to facilitate the study of a large number of SP_n structures. With the help of this notation the structures investigated in this paper are partitioned into classes and families. The families with sizable photonic band gaps are analyzed in detail and an optimized set of parameters is determined in each case.

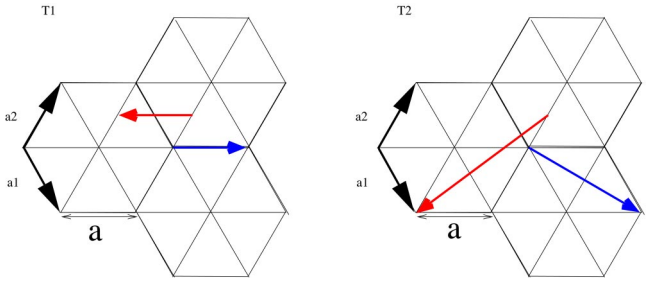

FIG. 5. (Color online) Top view of the $T_{2p}^{(1)}$ and $T_{2p}^{(2)}$ structures. The arrows in the figure represent the pores which start on plane $z=0$ and end on plane $z=c$. For a perspective view of $T_{2p}^{(2)}$ see Fig. 3.

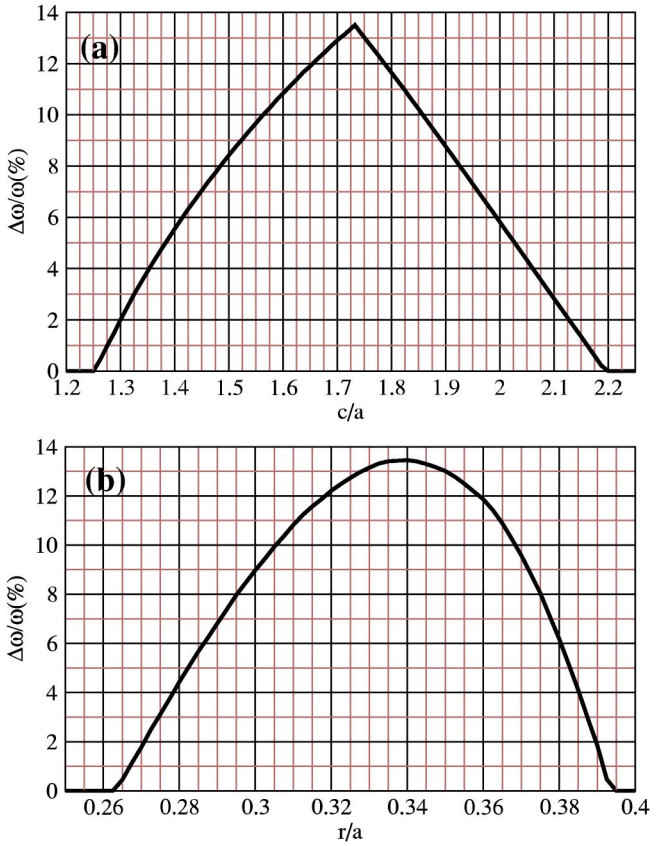

FIG. 6. $T/[1,1]\oplus[-1,-1]^{(0,0.5)}$ family of photonic crystals. (a) Relative size of the full photonic band gap as a function of c for $r=0.34a$. (b) Relative size of the full photonic band gap as a function of r for $c=1.73a$. The dielectric constant of the background material is 11.9.

II. DESCRIPTION OF THE SP_n PHOTONIC CRYSTALS

A photonic crystal belonging the to SP_n class can be described using a two-dimensional lattice (the mask) and n pore axes ("drilling directions") associated with each unit cell of the mask. Figure 1 displays an example of a SP_1 structure based on a square mask. The primitive vectors of the mask lattice are $\vec{a}_1=(a,0,0)$ and $\vec{a}_2=(0,a,0)$ where a is the lattice constant of the mask. $\vec{c}$ is a vector perpendicular to the mask plane and its length c, is unrelated to a. A pore (illustrated in Fig. 1 as a cylinder) associated with mask point P, is defined by its in-plane shift relative to P, $\vec{\delta}=\delta_1\vec{a}_1+\delta_2\vec{a}_2$ $(0\leqslant\delta_1,\delta_2<1)$; its projection on the mask plane, $n_1\vec{a}_1+n_2\vec{a}_2$ (n_1 and n_2 are integers); its vertical displacement c. We denote this pore by the symbol $[n_1,n_2]^{(\delta_1,\delta_2)}$ or simply $[n_1,n_2]$ when $\vec{\delta}=\vec{0}$. Extending the pores to infinite length is equivalent to stacking the layer described above vertically with a periodicity of c. The resulting 3D periodic structure has a tetragonal Bravais lattice and the basis shown in Fig. 1. The tetragonal lattice is characterized by lattice constants a and c in plane and perpendicular to the plane, respectively. With the notation introduced above the SP_n class is further partitioned in families of structures denoted by $M/[n_1^1,n_2^1]^{(\delta_1^1,\delta_2^1)}\oplus\cdots\oplus[n_1^n,n_2^n]^{(\delta_1^n,\delta_2^n)}$, where M denotes the

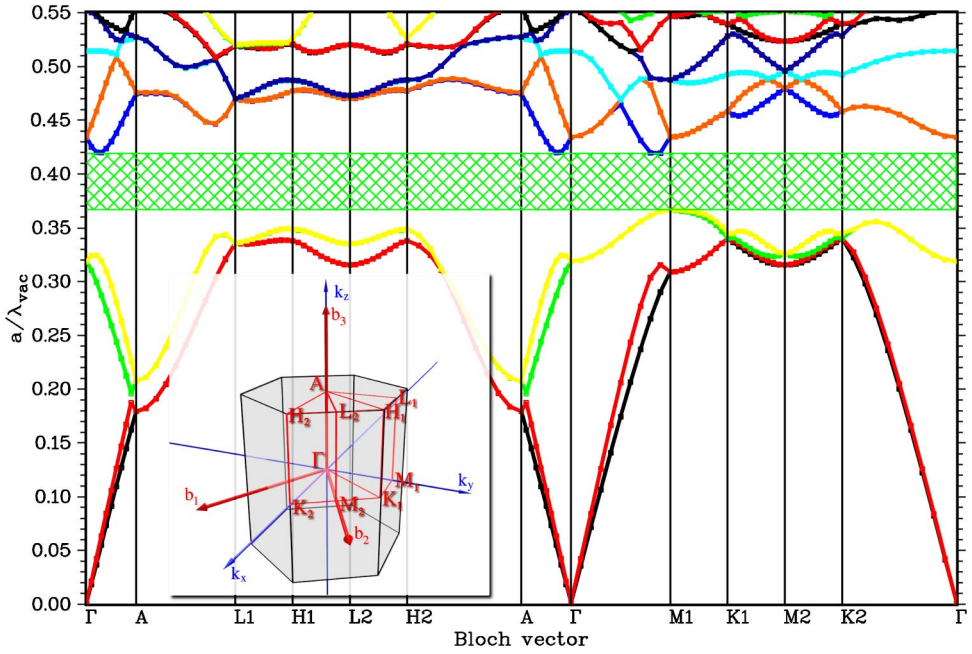

FIG. 7. (Color online) Photonic band structure for the optimized $T/[1,1]\oplus[-1,-1]^{(0,0.5)}$ photonic crystal characterized by c=1.73a and r=0.34a. The air volume filling fraction is 80.47% and the full photonic band gap opens between bands 4 and 5 of the hexagonal photonic band structure. The relative size of the gap is 13.5% and it is centered at a/λ_{vac}=0.39. The inset shows the positions of the high symmetry points in the hexagonal Brillouin zone.

type of the mask (S for square, T for triangular) and $[n_1^k, n_2^k]^{(\delta_1^k, \delta_2^k)}$ describes the kth pore axis. The structures belonging to such a family are distinguished by the radius of the pores r, and the pore's vertical displacement c. A photonic crystal obtained by drilling holes of radius r along these pore axes in a solid background belongs to the corresponding SP_n family. As an illustration, the simple SP_1 structure displayed in Fig. 1 belongs to family $S/[1,1]^{(0.5,0.5)}$.

An example of a SP_2 structure based on a square mask is shown in Fig. 2. In this case the first pore axis runs in direction $1\vec{a}_1+1\vec{a}_2+\vec{c}$ and the second, shifted by an in plane vector $\vec{\delta}=0.5\vec{a}_1+0\vec{a}_2$, in direction $-1\vec{a}_1-1\vec{a}_2+\vec{c}$. This SP_2 structure belongs to family $\boldsymbol{S}/[1,1]\oplus[-1,-1]^{(0.5,0)}$. Here again $\boldsymbol{S}$ denotes the type of the mask (square), $[1,1]\equiv[1,1]^{(0.0)}$ indicates that the first pore runs from (0, 0, 0) to $1\vec{a}_1+1\vec{a}_2+\vec{c}$ and $[-1,-1]^{(0.5,0)}$ indicates that the second pore runs from $\vec{\delta}=0.5\vec{a}_1+0\vec{a}_2$ to $\vec{\delta}-1\vec{a}_1-1\vec{a}_2+\vec{c}$.

Similar notations can be used for SP_n structures with $n>2$ or different masks. Two examples of SP_n structures based on triangular masks are shown in Figs. 3 and 4. With the choice of the mask primitive vectors as $\vec{a}_{1,2}=(1/2a, \mp\sqrt{3}/2a, 0)$ the two structures correspond to $T/[2,1]\oplus[-1,-2]^{(0,0.5)}\in SP_2$ and $T/[2,1]\oplus[-1,1]\oplus[-1,-2]\in SP_3$, respectively. We note that the Yablonovite photonic crystal [44] belongs to the $T/[2,1]\oplus[-1,1]\oplus[-1,-2]$ family and corresponds to $c=\sqrt{6}a$.

The notation introduced above is not unique. Identical SP_n structures can be labeled differently depending on the choice of the primitive vectors and the z coordinate of the mask plane.

III. SP_2 CLASS OF PHOTONIC CRYSTALS

All the members of the SP_1 family are in fact 2D photonic crystals. They were used in Sec. II only as an illustration of the notation scheme. In the rest of the paper we will focus on 3D photonic crystals and we start the study with the simplest nontrivial class SP_2.

We find two distinct SP_2 structures based on a triangular mask which exhibit photonic band gaps. These structures are $T_{2p}^{(1)}\equiv T/[1,1]\oplus[-1,-1]^{(0,0.5)}$ and $T_{2p}^{(2)}\equiv T/[2,1]\oplus[-1,-2]^{(0,0.5)}$. Figure 5 illustrates schematically the position and orientation of the pores for the two structures while Fig. 3 shows a perspective view of $T_{2p}^{(2)}$. Members of the two families described above are distinguished by the radius of the pores r and the vertical pitch c. For both of these families we calculated photonic band structures for a large number of (c, r) points in the parameter space. The photonic band structures were calculated using the plane wave method [31] with an expansion of more than 1400 plane waves. For all the structures we used a dielectric constant of 11.9 for the background material. Figure 6(a) shows the dependence of the full photonic band gap of $T_{2p}^{(1)}$ as a function of c for r =0.34a. The photonic band gap remains open for 1.25a<c <2.2a and reaches its peak at c=1.73a. The slope of the curve shown in Fig. 6(a) is discontinuous because the photonic band gap corresponding to different c values closes at different points in the Brillouin zone. The volume filling fraction of the pores (air) varies from 87.35% at c=1.25a to 77.35% at c=2.2a. Figure 6(b) shows the dependence of the full photonic band gap of $T_{2p}^{(1)}$ as a function of r for c =1.73a. The gap remains open for 0.265a<r<0.395a. The

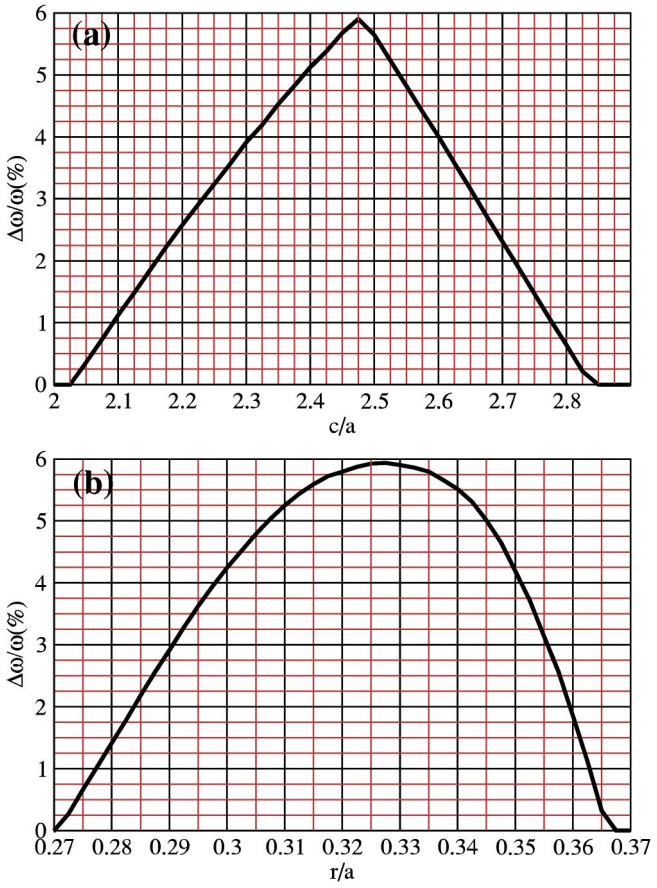

FIG. 8. $T/[2,1]\oplus[-1,-2]^{(0,0.5)}$ family of photonic crystals. (a) Relative size of the full photonic band gap as a function of c for $r=0.33$a. (b) Relative size of the full photonic band gap as a function of r for c=2.475a. The dielectric constant of the background material is 11.9.

volume filling fraction of the pores (air) varies from 56.65% at $r=0.265$a to 93.45% at $r=0.395$a. Figure 7 shows the photonic band structure of the optimized $T_{2p}^{(1)}$ photonic crystal characterized by c=1.73a and $r=0.34$a. The volume filling fraction of the pores for this optimized structure is 80.47%. The photonic band gap opens between bands 4 and 5 of the hexagonal photonic band structure. The relative size of the photonic band gap is 13.5% and it is centered at $\omega a/2\pi c = a/\lambda_{vac}=0.39$ (c is the speed of light). The inset shows the irreducible Brillouin zone together with the positions of the high symmetry points used in the calculations. For all the structures studied in this paper we have also determined quantitatively the degree of overlap between the pores. This overlap is expressed in percent and is defined as $(\mathcal{V}_{\text{pores}}/\mathcal{V}_{\text{pores network}}-1)/n$ where $\mathcal{V}_{\text{pores network}}$ is the volume of the pores network, $\mathcal{V}_{\text{pores}}$ is the volume of all the pores as if they were disjoint, and n is the number of pores per mask point. $\mathcal{V}_{\text{pores}}$ is greater than or equal to $\mathcal{V}_{\text{pores network}}$. When the two volumes are equal the pores of the SP_n structure are disjoint and the overlap is 0%. For the optimized $T_{2p}^{(1)}$ structure the overlap is 10% and it varies from 2% to 20% when c=1.73a and $0.265\text{a}\leqslant r\leqslant 0.395$a.

Similar calculations have been performed for the $T_{2p}^{(2)}=T/[2,1]\oplus[-1,-2]^{(0,0.5)}$ structure which differs from $T_{2p}^{(1)}$ in

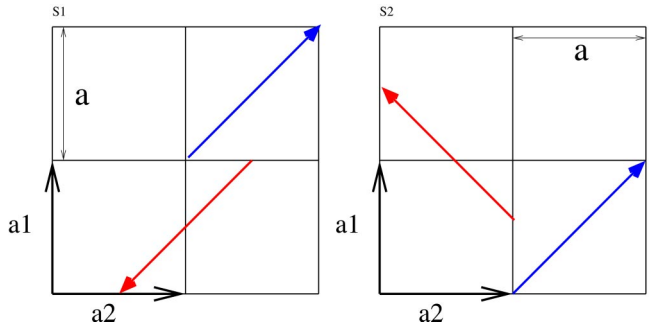

FIG. 9. (Color online) Top view of the $S_{2p}^{(1)}$ and $S_{2p}^{(2)}$ pore structures. The arrows in the figure represent the pores which start on plane $z=0$ and end on plane $z=$c. For a perspective view of the pores of $S_{2p}^{(1)}$ see Fig. 2.

the orientation of the two pores relative to the mask (see Fig. 5). Figure 8(a) shows the variation of the relative size of the full photonic band gap as a function of c for $r=0.33$a. The volume filling fraction of the pores varies from 83.46% at c=2.00a to 77.11% at c=2.85a. Figure 8(b) shows the variation of the relative gap size as a function of r for c=2.47a. The volume filling fraction of the pores varies from 60.51% at $r=0.27$a to 89.41% at $r=0.37$a. The optimized $\boldsymbol{T}_{2p}^{(2)}$ photonic crystal, characterized by c=2.475a and $r=0.325$a, has a photonic band gap of only 6%. The volume filling fraction of the optimized structure is 77.9% and the overlap between the pores is 10%.

For the case of a square mask we find two distinct SP_2 families which exhibit large photonic band gaps: $S_{2p}^{(1)}\equiv S/[1,1]\oplus[-1,-1]^{(0.5,0)}$ and $S_{2p}^{(2)}\equiv S/[1,1]\oplus[-1,1]^{(0,0.5)}$. Figure 9 displays schematically the position and orientation of the pores of both these structures while Fig. 10 displays a three-dimensional perspective of the optimized $S_{2p}^{(1)}$ crystal. For the specific choice of $c=\sqrt{2}$a, the $S_{2p}^{(1)}$ structure resembles an inverted "woodpile" [32,35,36] crystal, consisting of circular air rods in a solid background. The pore axes do not cross each other but the pores can overlap if their radius is sufficiently large. In the case of the optimized $S_{2p}^{(1)}$, $r=0.345$a, it is the overlap of the pores which leads to a larger PBG than in conventional "woodpile" structures created through layer by layer growth. The SP_n structures can also be described using an alternative scheme which is more appropriate for a multistage fabrication process in which the pores are created sequentially. For example the $S/[1,1]\oplus[-1,-1]^{(0.5,0)}$ structure can be described by two square masks, displaced by (a/2,0), each having a single pore associated with it (see the inset of Fig. 10). We studied the dependence of the photonic band structure of the $S_{2p}^{(1)}$ photonic crystals made from Si ($\varepsilon=11.9$) as a function of c and the radius of the pores r. We find the optimized structure to be characterized by c=1.40a and $r=0.345$a. For this optimized geometry the volume filling fraction of the pores is 80.16% and the full photonic band gap, centered at $\omega a/2\pi c=a/\lambda_{vac}=0.41$, has a relative size of $\Delta\omega/\omega=24\%$. Figure 11 shows the photonic band structure of the optimized $S_{2p}^{(1)}$ photonic crystal calculated using the plane wave method. The inset shows the irreducible Brillouin zone together with the positions of the symmetry points used in the calculations.

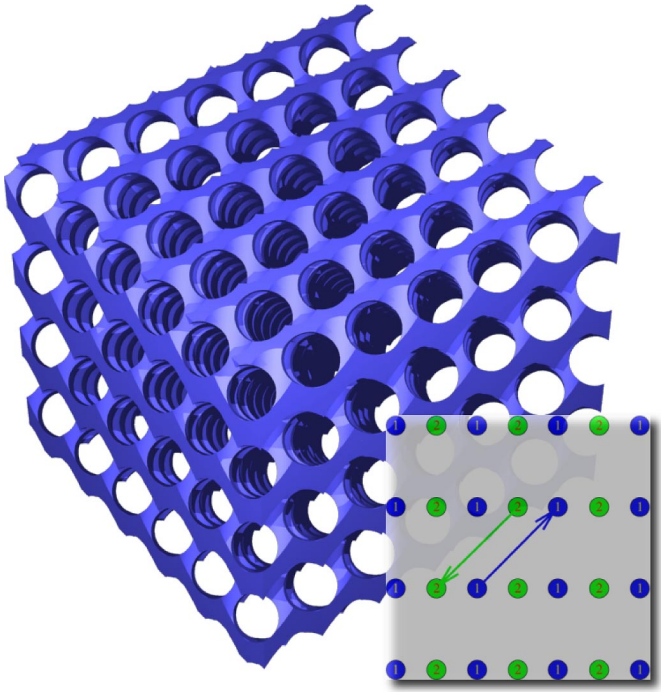

FIG. 10. (Color online) The optimized silicon $S/[1,1]\oplus[-1,-1]^{(0.5,0)}$ photonic crystal. The radius of the pores is $r=0.345$a and c=1.40a. The volume filling fraction of the pores is 80.16% and the full photonic band gap has a relative size of 24%. The inset shows an alternative view of the pore configuration for the $S/[1,1]\oplus[-1,-1]^{(0.5,0)}$ family. The photonic band structure of this photonic crystal is shown in Fig. 11.

Figure 12(a) shows the dependence of the relative size of the photonic band gap as a function of c for a fixed pore radius of $r=0.345$a. We find the full photonic band gap to be robust to changes in c. The full photonic band gap remains open for $0.9\text{a}<\text{c}<2.2\text{a}$ while the pore volume fraction varies from 94.37% at c=0.9a to 70.60% at c=2.2a. The discontinuous character of the slope of the curve plotted in Fig. 12(a) is explained by the fact that as c increases from 0.9a to 2.2a the upper edge of the photonic band gap closes at different symmetry points of the Brillouin zone, M_1, R_1, Γ (see Fig. 11) and thus the relative gap size acquires a different c dependence on different segments. A full photonic band gap of more than 21% exists for $1.1\text{a}<\text{c}<1.6\text{a}$ corresponding to a relative angle between pores ranging from 104° to 83°. The overlap between pores varies between 20% at c=1.1a to 15% at c=1.6a. For $r=0.345$a, the photonic band gap remains nonzero for a relative angle in the very broad range of 66° to 115°.

Figure 12(b) shows the dependence of the relative size of the full photonic band gap as a function of the pore's radius r for a fixed c=1.40a. The background material is Si ($\varepsilon=11.9$). We also find the full photonic band gap to be quite robust with respect to changes in r. The gap remains open for $0.20\text{a}<r<0.42\text{a}$ and the air volume fraction varies from 35.3% at $r=0.20$a to 95.5% at $r=0.42$a. For all values of r the upper edge of the photonic band gap closes at point R_1 (see Fig. 11). A full photonic band gap of more than 20% exists for $0.30\text{a}<r<0.38\text{a}$ and the overlap between the pores varies between 10% at $r=0.30$a to 23% at $r=0.38$a.

We have also studied the "inverted" $S_{2p}^{(1)}$ family which consists of solid Si cylinders ($\varepsilon=11.9$) in air. The optimized photonic crystal in this case is characterized by c=1.6a and $r=0.19$a. The volume filling fraction of the cylinders is 30.6% and the relative size of the full photonic band gap is 16% (in agreement with the results reported in [32]). The gap in this case opens also between bands 4 and 5 of the tetragonal photonic band structure and is centered at $\text{a}/\lambda_{\text{vac}}=0.35$. For the optimized inverted $S_{2p}^{(1)}$ structure the overlap between cylinders is very small.

A similar study was performed for the $S_{2p}^{(2)}$ structure. Here we find that the optimized photonic crystal is characterized by c=a, $r=0.305$a and the relative size of the photonic band gap, centered at $\text{a}/\lambda_{\text{vac}}=0.47$, is 21% (see Fig. 13). The pore

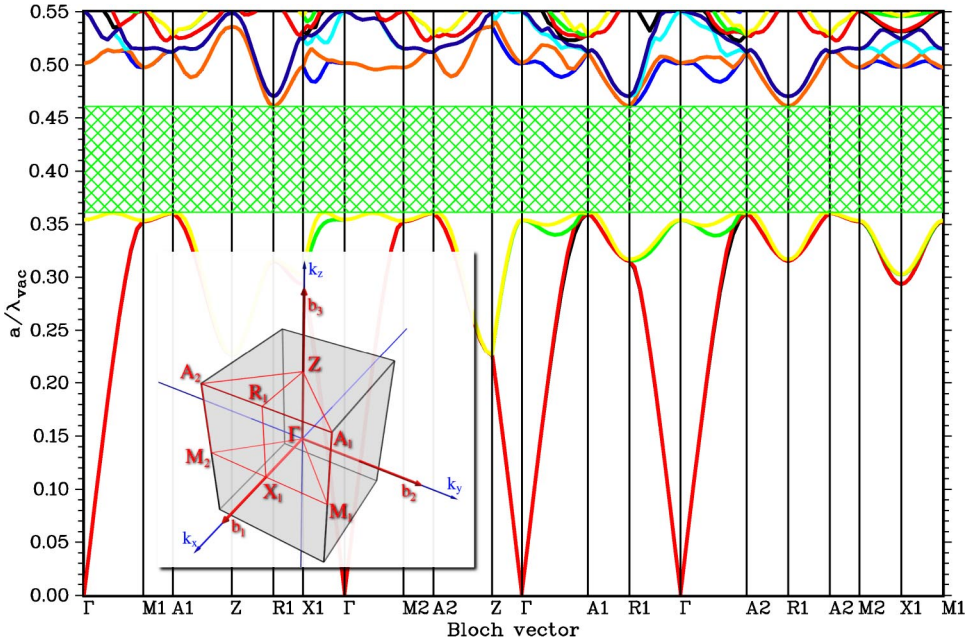

FIG. 11. (Color online) Band structure of the optimized $S_{2p}^{(1)}$ photonic crystal. The crystal is characterized by c=1.40a and $r=0.345$a. The volume filling fraction of the pores is 80.16% and the overlap between pores is 16%. The full photonic band gap is centered at $\text{a}/\lambda_{\text{vac}}=0.41$, opens between bands 4 and 5 of the tetragonal photonic band structure, and has relative size 24%. The position of the irreducible Brillouin zone symmetry points is illustrated in the inset.

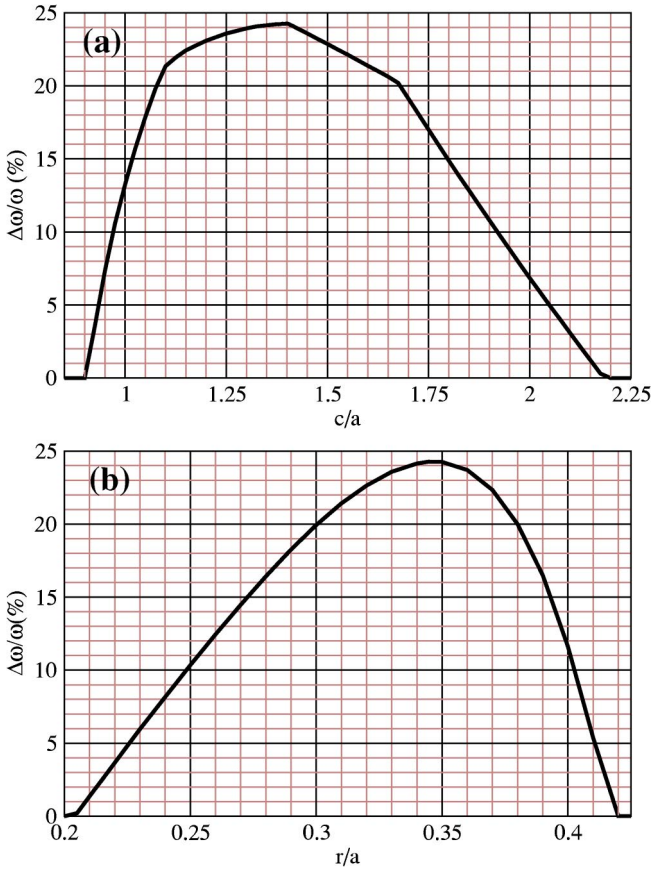

FIG. 12. $S_{2p}^{(1)}$ family of photonic crystals. (a) Relative size of the full photonic band gap as a function of c for $r=0.345$a. (b) Relative size of the full photonic band gap as a function of the pore radius r for c=1.40a. The dielectric constant of the background material is 11.9.

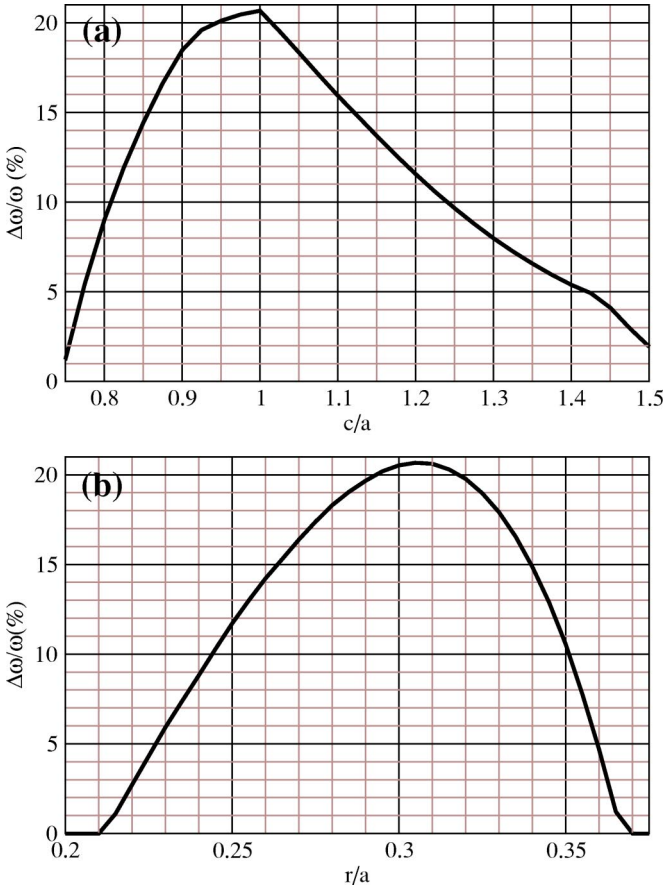

FIG. 13. $S_{2p}^{(2)}$ family of photonic crystals. (a) Relative size of the full photonic band gap as a function of c for $r=0.305$a. (b) Relative size of the full photonic band gap as a function of the pore radius r for c=1.0a. The dielectric constant of the background material is 11.9.

volume filling fraction is 80% and the overlap between the pores in this case is 13%. When c=a (cubic Bravais lattice) the $S/[1,1]\oplus[-1,1]^{(0,0.5)}$ structure is also a member of the $S/[1,1]\oplus[-1,-1]^{(0.5,0)}$ family and thus we find that the optimized SP_2 photonic crystal based on a square mask belongs to the $S_{2p}^{(1)}$ family.

IV. GENERALIZED DESCRIPTION FOR SP_2 STRUCTURES

For some fabrication techniques such as photoelectrochemistry it is advantageous to use "vertical drilling" for creating pores in a solid material. In principle all SP_n structures can be manufactured in this way provided that the solid can be "polished" after each etching step to provide faces normal to prescribed directions for the subsequent etching step. We illustrate this alternative description on the SP_2 family based on rhombohedral lattice masks $R_{2p}^{(1)} \equiv R/[1,1]\oplus[-1,-1]^{(0.5,0)}$. The standard mask is displayed in Fig. 14. The primitive vectors of the $R_{2p}^{(1)}$ mask lattice have equal length and make an angle θ with the x axis:

$$\vec{a}_1 = a(\cos(\theta), -\sin(\theta)),$$

$$\vec{a}_2 = a(\cos(\theta), \sin(\theta)).$$

The $R_{2p}^{(1)}$ family is a superset of the SP_2 families studied in the previous sections. The square and triangular families correspond to $\theta=45°$ and $\theta=60°$, respectively. The angle γ between the pore directions in this case (see the inset of Fig. 14) is given by

$$\cos(\gamma) = [c^2 - 4a^2\cos^2(\theta)]/[c^2 + 4a^2\cos^2(\theta)]. \qquad (1)$$

In the alternative description we consider two planes that are perpendicular to the two sets of pores. These are the so-called "polished faces" and we describe the structure in terms of the intersections between the polished face and the corresponding set of normal pores.

Figure 15 displays a "polished chunk" of the previously studied $S_{2p}^{(1)}$ structure (which belongs to the $\theta=45°$ $R_{2p}^{(1)}$family) when $c=\sqrt{2}a$. According to Eq. (1) the pore directions in this case are perpendicular to each other. The polished faces (labeled by a and b in Fig. 15) are perpendicular to the $(1,1,\sqrt{2})$ and $(-1,-1,\sqrt{2})$ directions, respectively. For a general $R_{2p}^{(1)}$ structure a face is intersected at normal angle by one set of pores and at an oblique angle by

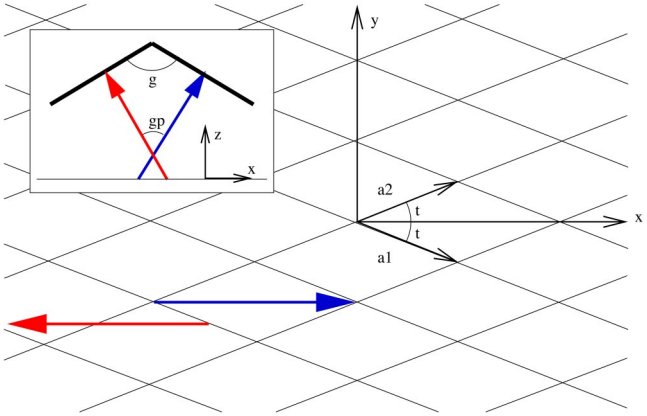

FIG. 14. (Color online) The standard mask used for a rhombohedral $R/[1,1]\oplus[-1,-1]^{(0.5,0)}$ SP_2 structure. The primitive vectors have equal length a and make equal angles θ with the x axis. The directions of the two pores are also illustrated. The inset shows a side view of the pores. γ is the angle made by two planes perpendicular to the pore directions.

the other. When $\gamma=90°$ (the case illustrated in Fig. 15) the pores are either normal or parallel to the faces.

In general, the intersections between the polished faces and the normal pores form 2D lattices like the ones sketched in Fig. 16. One could always choose face a such that one row of lattice points is right on the edge where the planes of the polished faces intersect. We choose O to be such a point, common to both faces, which provides a reference position (see Figs. 15 and 16) and consider that the position on each face is measured relative to its own two-dimensional coordinate system (x_0,y_0) centered at O.

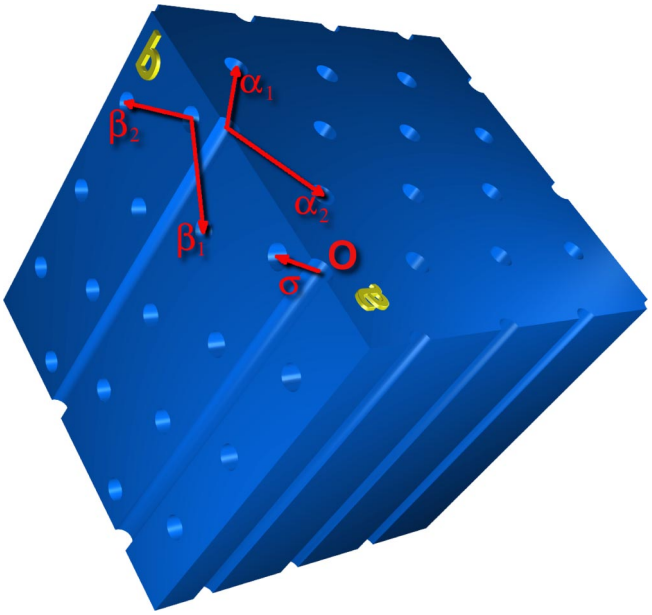

FIG. 15. (Color online) Alternative view of the $S/[1,1]\oplus[-1,-1]^{(0.5,0)}$ structure when $c=\sqrt{2}a$. The solid material is polished such that faces perpendicular to the two mutually perpendicular sets of pores are created. The annotations displayed on faces a and b are used to describe the intersections between the faces and pores, which are illustrated in Fig. 16.

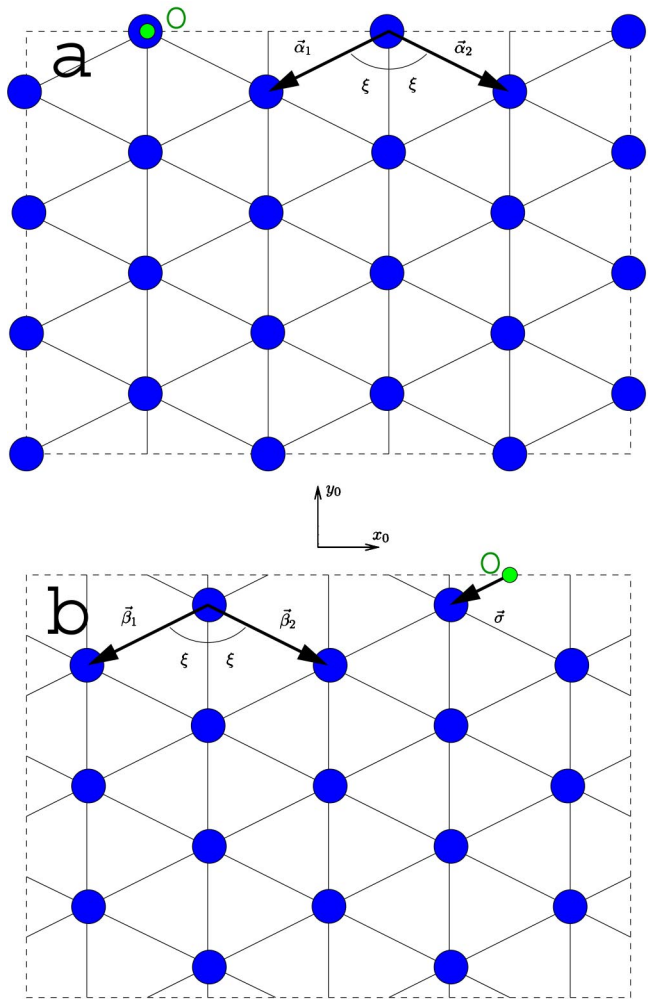

FIG. 16. (Color online) a and b are the planes of the two "polished faces" of a generic $R^{(1)}_{2p}$ structure (see also Fig. 15 for a specific example). The intersections between a face and the set of corresponding normal pores form a 2D rhombohedral lattice whose primitive vectors are illustrated. O is the point common to the two intersecting faces (see Fig. 15). The coordinates on each face are measured relative to a Cartesian coordinate system centered at O, whose axes are parallel to (x_0,y_0).

In the case of the general $R^{(1)}_{2p}$ structure it can be shown that the positions of the intersections between face a and the set of normal pores are given by $\{n_1\vec{\alpha}_1+n_2\vec{\alpha}_2;n_1,n_2\in Z\}$ while the intersections between face b and its set of normal pores are given by $\{\vec{\sigma}+m_1\vec{\beta}_1+m_2\vec{\beta}_2;m_1,m_2\in Z\}$. $\vec{\alpha}_{1,2}$, and $\vec{\beta}_{1,2}$ are the primitive vectors of the 2D rhombohedral lattices formed on faces a and b, respectively (see Fig. 16) and are given in terms of the standard SP_2 parameters (see Fig. 14) by

$$\vec{\alpha}_1=\vec{\beta}_1=a\left(-\sin(\theta),\frac{-c\cos(\theta)}{\sqrt{c^2+4a^2\cos^2(\theta)}}\right), \tag{2}$$

$$\vec{\alpha}_2=\vec{\beta}_2=a\left(\sin(\theta),\frac{-c\cos(\theta)}{\sqrt{c^2+4a^2\cos^2(\theta)}}\right), \tag{3}$$

and

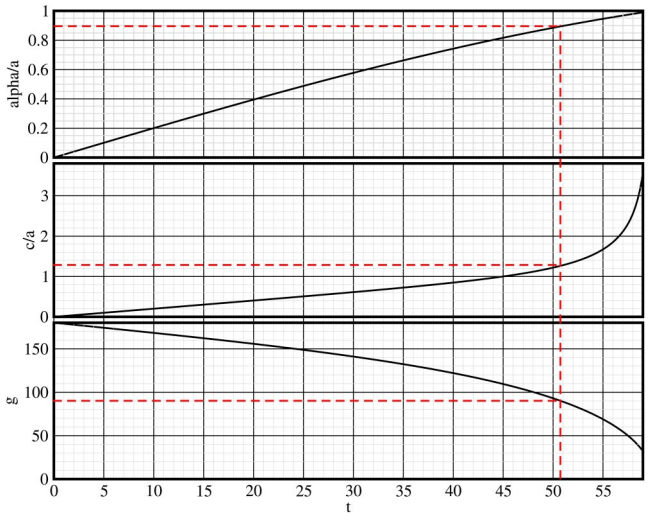

FIG. 17. (Color online) The dependence of c/a [Eq. (7)], γ [Eq. (1)], and a_r/a [Eq. (5)] on θ (see Fig. 14) for a $R_{2p}^{(1)}$ structure whose intersections between the pores and the face perpendicular to them form a 2D hcp lattice. The values for $\gamma=90°$ are highlighted.

$$\vec{\sigma} = \frac{\vec{\beta}_1}{2}. \tag{4}$$

According to Eqs. (2) and (3) the lattices on the two faces are identical and the lengths of their primitive vectors are

$$a_r = |\vec{\alpha}_i| = |\vec{\beta}_i| = a\sqrt{\frac{c^2 + a^2\sin^2(2\theta)}{c^2 + 4a^2\cos^2(\theta)}}. \tag{5}$$

Half the angle between the primitive vectors of the polished face, ξ in Fig. 16, is given by

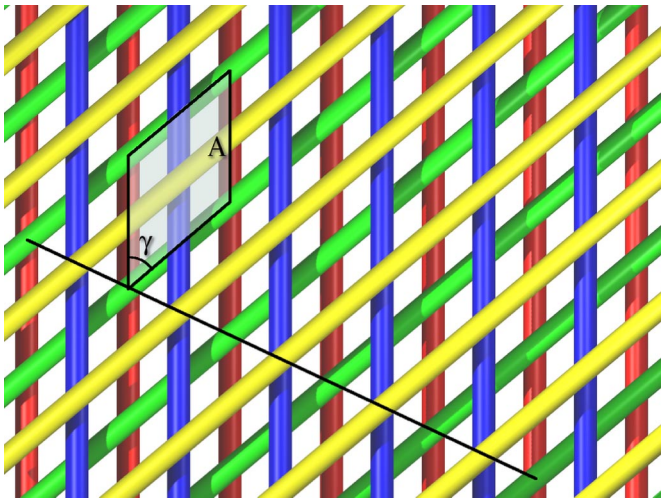

FIG. 18. (Color online) The transversal stacking sequence for a $R_{2p}^{(1)}$ structure as seen from a direction which is parallel to the *xy* plane of Fig. 14. The profile of that plane together with the two pore directions are also illustrated. γ is the angle between the pore directions. The transversal cross section of the crystal's monoclinic unit cell is highlighted.

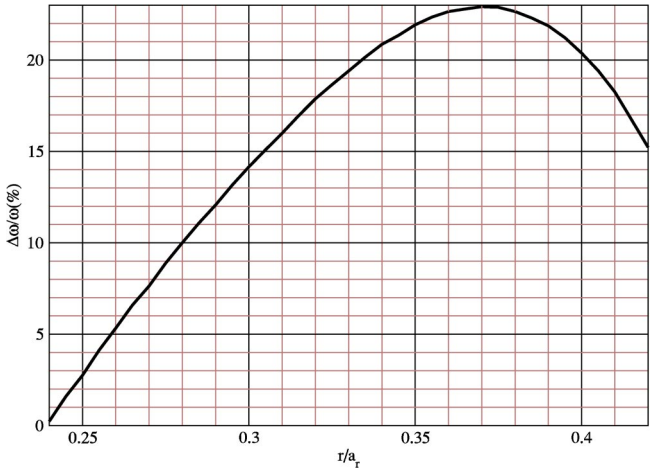

FIG. 19. The dependence of the relative size of the full photonic band gap as a function of the radius of the pores for a $R_{2p}^{(1)}$ structure created using vertical pores drilling from 2D hcp lattices on perpendicular faces. a_r is the lattice constant of the hcp lattices.

$$\cos(\xi) = \cos(\theta)\frac{c}{\sqrt{c^2 + a^2\sin^2(2\theta)}}. \tag{6}$$

A constraint imposed on the type of lattice formed by the intersections between the polished face and the corresponding set of normal pores implies a constraint among the standard parameters a, θ, and c. For example, a 2D square lattice on the polished face, defined by $\xi=\pi/4$, would require

$$c = a\frac{\sin(2\theta)}{\sqrt{\cos(2\theta)}}.$$

Similarly, in order to obtain a hexagonal close-packed (hcp) 2D lattice, defined by $\xi=\pi/3$, the following has to be satisfied:

$$c = a\frac{\sin(2\theta)}{\sqrt{1 + 2\cos(2\theta)}}. \tag{7}$$

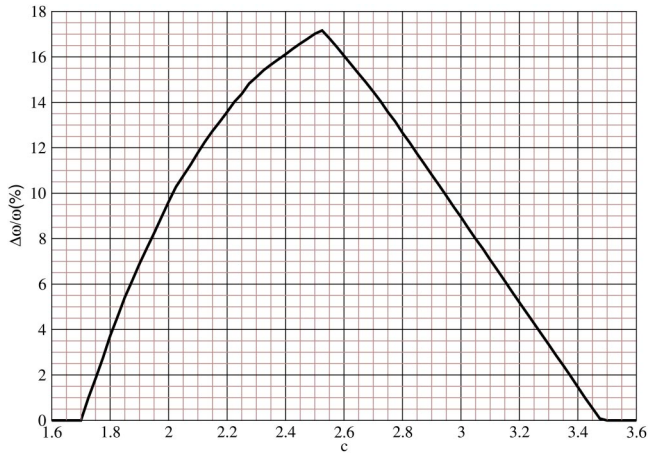

FIG. 20. Relative size of the full photonic band gap as a function of c (measured in units of a) for the $T/[2,1]\oplus[-1,1]\oplus[-1,-2]$ structure characterized by $r=0.335a$.

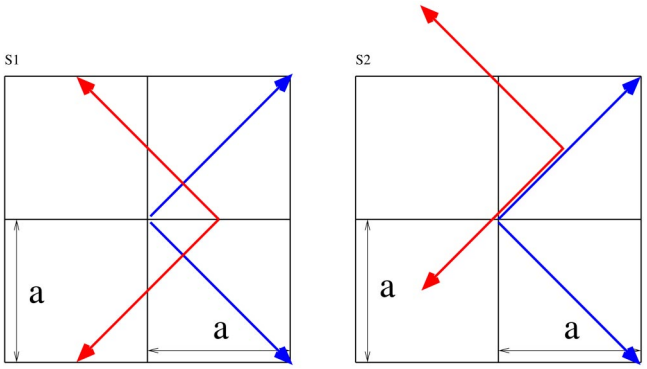

FIG. 21. (Color online) Top view of the $S_{4p}^{(1)}$ and $S_{4p}^{(2)}$ structures. The arrows in the figure represent the pores which start on plane $z=0$ and end on plane $z=c$.

Figure 17 shows as an example the dependence of c/a [Eq. (7)], γ [Eq. (1)], and a_r/a [Eq. (5)] on the angle θ (see Fig. 14] in the case when the lattice on the polished faces is 2D hcp. θ is restricted to the interval $[0, \pi/3]$. The values corresponding to $\gamma=90°$ (perpendicular polished faces) are highlighted in the plot and they correspond to a SP_2 structure which does not belong to the S or T family studied in the previous sections ($\theta \approx 51°$). Also from Fig. 17 we find that in order to obtain hcp lattices on the polished faces from an $S_{2p}^{(1)}$ structure ($\theta=45°$) the angle between the polished faces should be $\gamma \approx 110°$ and $c=a$. From the data shown in Fig. 12(a) we find that in this case the optimized structure would have a full photonic band gap of only $\approx 14\%$.

For a manufacturing process involving the growth of pores from the surface of the polished faces it is important to approach the design optimization problem from a different perspective. Given the type of the lattice on the polished faces (the angle ξ in Fig. 16) and the angle between them (γ), find the radius of the pores that generates the structure with the largest full photonic band gap. Figure 18 displays the transverse stacking sequence of pores for a generic $R_{2p}^{(1)}$ structure. This "skewed woodpile" has a monoclinic unit cell whose rhombohedral face is highlighted in Fig. 18. This

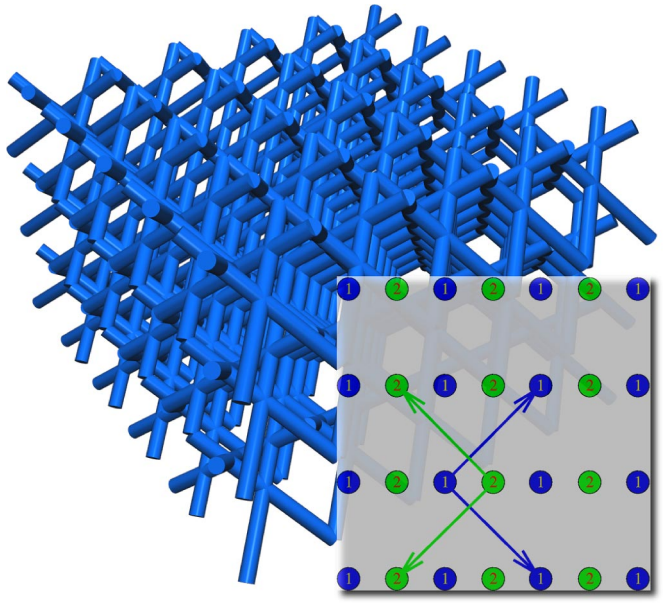

FIG. 22. (Color online) The network formed by the pores of the $S_{4p}^{(1)}$ structure. The photonic crystal illustrated corresponds to $r=0.08a$ and $c=1.1a$. The inset displays the two masks and the pores configuration for the entire $S_{4p}^{(1)}$ family.

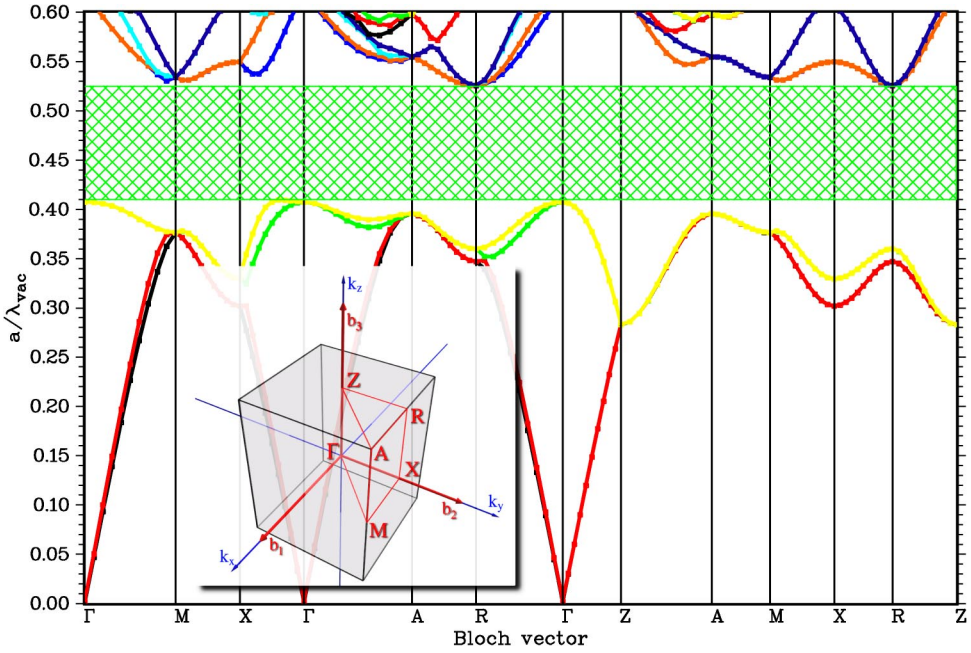

FIG. 23. (Color online) Band structure for the optimized $S_{4p}^{(1)}$ photonic crystal. The crystal is characterized by $c=1.10a$ and $r=0.31a$. The volume filling fraction of the pores is 81.51%. The full photonic band gap is centered at $a/\lambda_{vac}=0.47$, opens between bands 4 and 5 of the tetragonal photonic band structure, and has relative size 25%. The positions of the irreducible Brillouin zone symmetry points are illustrated in the inset.

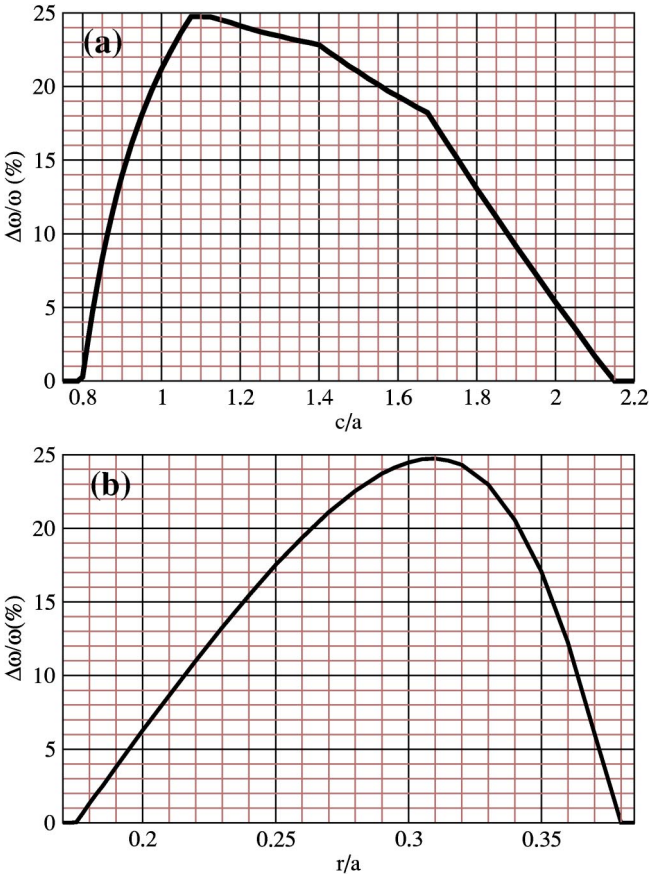

FIG. 24. $S_{4p}^{(1)}$ family of photonic crystals. (a) Relative size of the photonic band gap as a function of c for $r=0.31$a. The gap remains open for $0.8\text{a} \leqslant \text{c} \leqslant 2.1\text{a}$ and on this interval the pore volume filling fraction varies between 93.3% and 69.2%. (b) Relative size of the photonic band gap as a function of the pore radius r for $\text{c}=1.10\text{a}$. On the interval $0.175\text{a} \leqslant r \leqslant 0.38\text{a}$ the volume filling fraction of the pores varies from 40.26% to 95.71% and the overlap between pores varies from 14% to 52%. The dielectric constant of the background material is 11.9.

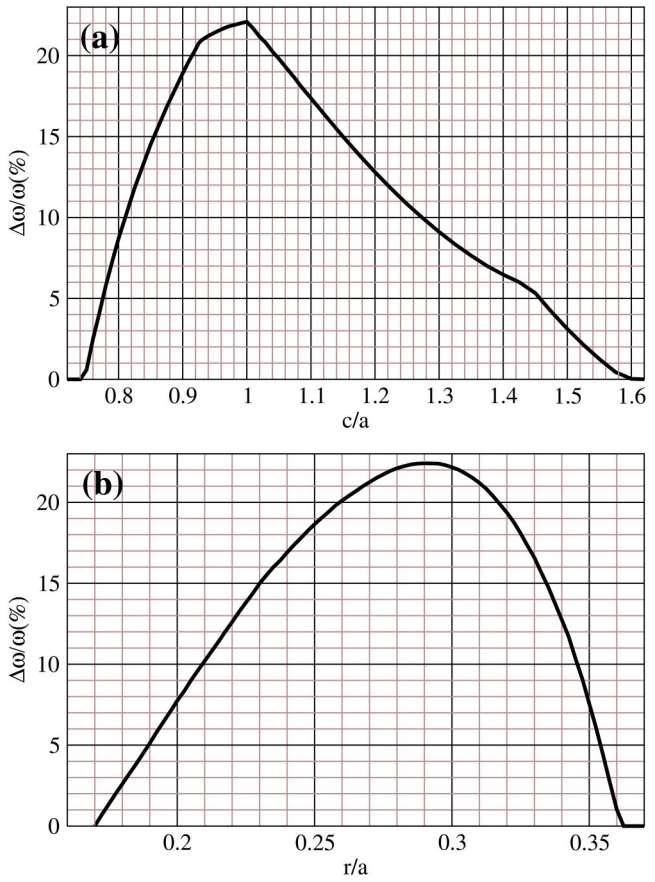

FIG. 25. $S_{4p}^{(2)}$ family of photonic crystals. (a) Relative size of the full photonic band gap as a function of c for $r=0.29$a. (b) Relative size of the full photonic band gap as a function of the pore radius r for $\text{c}=1.0$a. The dielectric constant of the background material is 11.9.

rhombohedron is characterized by angle γ and edge length A. The height of the monoclinic unit cell (its extent along the direction normal to the highlighted face) is denoted as C. If we use a_r [Eq. (5)] as the unit of length then

$$A = 2\text{a}_r \frac{\cos(\xi)}{\sin(\gamma)},$$

$$C = 2\text{a}_r \sin(\xi).$$

From symmetry considerations one expects that the size of the photonic band gap reaches its maximum value when $\gamma=90°$. Figure 19 shows the dependence of the relative size of the photonic band gap on the radius of the pores for a $R_{2p}^{(1)}$ structure created by vertical pore drilling from 2D hcp lattices on perpendicular polished faces. An optimal photonic band gap of 23% relative to center frequency is obtained for a background dielectric of 11.9. The optimum air filling fraction in this case is $\approx 80\%$. We limit our study to only the case of hcp lattices on the polished faces. For a report of the dependence of the photonic band gap size on the geometry of the polished face lattice we refer the reader to Ref. [49,50] where a similar structure has been investigated.

The results presented in this section illustrate the flexibility of the SP_2 design. Indeed, by removing the requirement of a high symmetry lattice mask (which characterizes the square and triangular SP_2 structures discussed in Sec. III) we extended our study to the case of the $R_{2p}^{(1)}$ family, an SP_2 structure whose lattice mask is rhombohedral. This family is a superset of the square and triangular SP_2 families and allows the use of masks for normal-to-surface drilling on the polished faces—a feature that may be very important for some manufacturing processes.

V. SP_3 CLASS OF PHOTONIC CRYSTALS

From the SP_3 class we studied only the $T/[2,1] \oplus [-1,1] \oplus [-1,-2]$ family to which the Yablonovite structure belongs. Figure 4 displays the position and orientation of the pores for this family. Because the pore axes of this family intersect all in the same point in space, it is expected that the overlap between pores will be large. The optimized $T/[2,1] \oplus [-1,1] \oplus [-1,-2]$ structure, characterized by c

$=2.525$ a and $r=0.335$ a, has an air volume fraction of 78.3% and an overlap between pores of 30%. This degree of overlap is significantly larger than the one of the SP_2 structures studied previously. Figure 20 shows the variation of the relative size of the full photonic band gap as a function of c for $r=0.335$ a. The full photonic band gapof the optimized crystal is approximately 17%.

VI. SP_4 CLASS OF PHOTONIC CRYSTALS

We find two distinct SP_4 families based on a square mask exhibiting large photonic band gaps: $S_{4p}^{(1)} \equiv S/([1,1] \oplus [1,-1]) \oplus ([-1,-1] \oplus [-1,1])^{(0.5,0)}$ and $S_{4p}^{(2)} \equiv S/([1,1] \oplus [1,-1]) \oplus ([-1,-1] \oplus [-1,1])^{(0.5,0.5)}$. In order to simplify the notation we collected the pores with the same displacement in parentheses. Figure 21 shows the pore configuration for these two families and Fig. 22 displays the pore network for a particular member of the $\boldsymbol{S}_{4p}^{(1)}$ family. These structures can also be described by means of two masks with two pores per mask point as illustrated in the inset of Fig. 22 for the $S_{4p}^{(1)}$ family.

We studied the dependence of the relative size of the full photonic band gap as a function of c and r and find the optimized Si $S_{4p}^{(1)}$ structure to be characterized by $c=1.10a$ and $r=0.31a$. The band structure of the optimized $S_{4p}^{(1)}$photonic crystal for a Si background ($\varepsilon=11.9$) is shown in Fig. 23. The full photonic band gap, centered at $a/\lambda_{vac}=0.47$, opens between bands 4 and 5 of the tetragonal photonic band structure and has a relative size of 25%. The pore volume filling fraction is 81.51% and the overlap between pores is at 35%. The dependence of the relative gap size on c for $r=0.31a$ is shown in Fig. 24(a). The gap is larger than 20% for $1.0a \leqslant c \leqslant 1.55a$. When c runs in this interval the volume filling fraction of the pores varies from 84.5% to 73.6% and the overlap between the pores varies from 37% to 30%. The dependence of the relative gap size on r for $c=1.10a$ is shown in Fig. 24(b). A gap of more than 20% remains open for $0.27a \leqslant r \leqslant 0.34a$. When r runs in this interval the volume filling fraction of the pores varies from 70.5% to 88.5% whereas the overlap between pores varies from 28% to 42%.

For the "inverted" $S_{4p}^{(1)}$ structure made from solid cylinders ($\varepsilon=11.9$) in air background we find the optimized photonic crystal to be characterized by $c=1.7a$ and $r=0.15a$. The photonic band gap in this case is centered at $a/\lambda_{vac}=0.35$ and spans a range of approximately 20% of the center frequency. The volume fraction of the cylinders (Si in this case) is 26% and the overlap between the cylinders is 10%.

We have also studied the dependence of the photonic band gap on the r and c parameters for the $S_{4p}^{(2)}$ structure. We find the optimized Si $S_{4p}^{(2)}$ structure to be characterized by $r=0.29a$ and $c=1.0a$. For these parameters the photonic band gap is centered at $a/\lambda_{vac}=0.46$ and spans approximately 22% of the center frequency. The volume filling fraction of the pores is 79.2% and the overlap between the pores is 33%. Figure 25(a) shows the dependence of the photonic band gap on c for $r=0.29a$ and Fig. 25(b) shows the dependence of the full photonic band gap on r for $c=1.0a$.

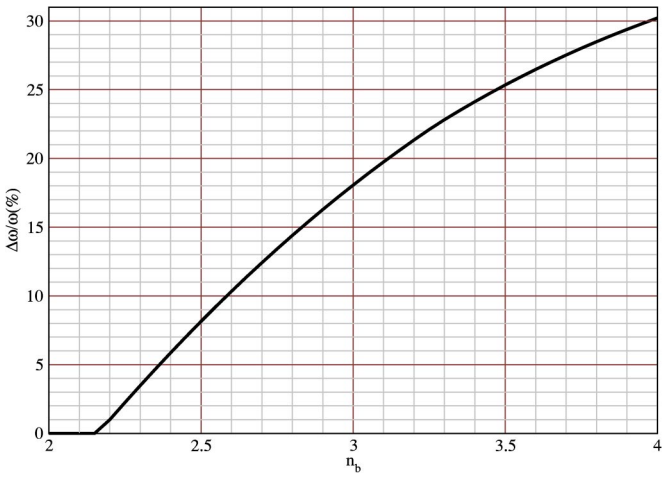

FIG. 26. Relative size of the full photonic band gap as a function of the index of refraction of the solid material (backround) for the $S_{4p}^{(1)}$ crystal characterized by $c=1.1a$ and $r=0.29a$. The index of refraction of the pores is 1.

Figure 26 shows the dependence of the relative size of the full photonic band gap of a $S_{4p}^{(1)}$ crystal characterized by $c=1.1a$ and $r=0.29a$ as a function of the index of refraction of the solid material (background in this case). The photonic band gap closes at an index of refraction $n_b \approx 2.15$. However, the structure that yields the largest photonic band gap is not the same structure that retains a photonic band gap for the smallest refractive index contrast. We find that if we allow the geometry of the photonic crystal to also change as the index of refraction is lowered then the gap can stay open for even lower values of n_b. Although we did not perform an exhaustive search of the minimum index of refraction constrast required for the photonic band gap to remain open, we found for example that for a solid index of refraction of 1.95 the gap is still open when $c=1.39a$ and $r=0.28a$.

VII. SUMMARY AND DISCUSSION

In summary, we have carried out an exhaustive study of slanted-pore photonic crystals and identified additional architectures for large 3D photonic band gaps in the near infrared (1.5 μm), suitable for ultrahigh resolution lithography. These architectures achieve close to the largest photonic band gaps ever predicted without the undesirable complexities of diamond lattice microfabrication. Given the prospect for nanometer scale precision in microfabrication, these PBG materials may open the door to nearly lossless optical microcircuitry and a variety of unusual quantum optical effects [29,30] involving photons and atoms placed within these structures.

LIGA method can be adapted to create point defects and optical waveguide channels within each of the four SP_n photonic crystal families described above. An optical microchip (containing prepatterned optical circuitry), in the form of a planar defect layer, may be introduced at the initial template stage by means of a "negative" or otherwise distinct photoresist that is impervious to the x rays used to expose the "positive" photoresists. The template for the microchip con-

sists of a thin (roughly 0.5a) membrane of photoresist that has been independently prepatterned as a 2D photonic crystal of solid rods with the periodicity of the mask lattices. Desired waveguide channels and microcavity defects may also be prepatterned as missing dielectric rods on this 2D membrane. The prepatterned "negative" or otherwise distinct photoresist is then sandwiched between a pair of unpatterned positive photoresists of thickness roughly 5*c*. After suitable alignment of an x-ray mask, the sandwich structure is now patterned as a SP_2 or SP_4 lattice in the regions of positive photoresist (as described above) by x-ray lithography. Alternatively, circuits of light can be created at the templating state by direct laser writing (two-photon absorption) techniques [12–15,51]. The template can then be replicated with silicon using a double inversion procedure. For example, it is posssible to invert the polymer template by room temperature chemical vapor deposition (CVD) of silica glass [52]. The resulting daughter template made of silica can withstand the heat of silicon CVD and inversion [42].

It has been demonstrated [25] that the optical waveguide modes of the membrane, if designed appropriately, will fall within the 3D PBG of the cladding layers, enabling broadband, lossless, and diffractionless flow of light within the microchip.

SP_2 structures can also be created using an alternative manufacturing process. As shown in Sec. IV, vertical "drilling" (using for example photoelectrochemical or reactive ion etching) combined with "polishing" can be used to create the two set of pores of a SP_2 structure. Any type of 2D lattice can be used as the seed pattern on the surface to be drilled. We showed that in the case of a 2D hexagonal close packed seed lattice the SP_2 structure can have a gap as large as 23% when the radius of the pores is appropriately chosen.

ACKNOWLEDGMENT

This work was supported in part by the Natural Sciences and Engineering Research Council of Canada.

[1] Sajeev John, Phys. Rev. Lett. **58**, 2486 (1987).
[2] Eli Yablonovitch, Phys. Rev. Lett. **58**, 2059 (1987).
[3] Ovidiu Toader, Mona Berciu, and Sajeev John, Phys. Rev. Lett. **90**, 233901 (2003).
[4] Wolfgang Ehrfeld and Andreas Schmidt, J. Vac. Sci. Technol. B **16**, 3526 (1998).
[5] K.-H. Brenner, M. Kufner, S. Kufner, J. Moisel, A. Müller, S. Sinzinger, M. Testorf, J. Göttert, and J. Mohr, Appl. Opt. **32**, 6464 (1993).
[6] C. Cuisin, Y. Chen, D. Decanini, A. Chelnokov, F. Carcenac, A. Madouri, J. M. Lourtioz, and H. Launois, J. Vac. Sci. Technol. B **17**, 3444 (1999).
[7] C. Cuisin, A. Chelnokov, J.-M. Lourtioz, D. Decanini, and Y. Chen, Appl. Phys. Lett. **77**, 770 (2000).
[8] C. Cuisin, A. Chelnokov, J.-M. Lourtioz, D. Decanini, and Y. Chen, J. Vac. Sci. Technol. B **18**, 3505 (2000).
[9] C. Cuisin, A. Chelnokov, D. Decanini, D. Peyrade, Y. Chen, and J. M. Lourtioz, Opt. Quantum Electron. **34**, 13 (2002).
[10] G. Feiertag *et al.*, Appl. Phys. Lett. **71**, 1441 (1997).
[11] F. Romanato *et al.*, Microelectron. Eng. **67-68**, 479 (2003).
[12] Shoji Maruo, Osamu Nakamura, and Satoshi Kawata, Opt. Lett. **22**, 132 (1997).
[13] Hong-Bo Sun, Shigeki Matsuo, and Hiroaki Misawa, Appl. Phys. Lett. **74**, 786 (1999).
[14] Brian H. Cumpston *et al.*, Nature (London) **398**, 51 (1999).
[15] Satoshi Kawata, Hong-Bo Sun, Tomokazu Tanaka, and Kenji Takada, Nature (London) **412**, 697 (2001).
[16] S. Ottow, V. Lehmann, and H. Föll, Appl. Phys. A: Mater. Sci. Process. **63**, 153 (1996).
[17] U. Grüning, V. Lehmann, and C. M. Engelhardt, Appl. Phys. Lett. **66**, 3254 (1995).
[18] A. Birner, R. B. Wehrspohn, U. M. Gösele, and K. Busch, Adv. Mater. (Weinheim, Ger.) **13**, 377 (2001).
[19] C. C. Cheng and Axel Scherer, J. Vac. Sci. Technol. B **13**, 2696 (1995).
[20] C. C. Cheng, Axel Scherer, V. Arbet-Engels, and E. Yablonovitch, J. Vac. Sci. Technol. B **14**, 4110 (1996).
[21] C. C. Cheng, V. Arbet-Engels, Axel Scherer, and E. Yablonovitch, Phys. Scr., T **68**, 17 (1996).
[22] K. Wang, A. Chelnokov, S. Rowson, P. Garoche, and J.-M. Lourtioz, J. Phys. D **33**, L119 (2000).
[23] A. Chelnokov, K. Wang, S. Rowson, P. Garoche, and J.-M. Lourtioz, Appl. Phys. Lett. **77**, 2943 (2000).
[24] J. R. Wendt, G. A. Vawter, P. L. Gourley, T. M. Brennan, and B. E. Hammons, J. Vac. Sci. Technol. B **11**, 2637 (1993).
[25] Alongkarn Chutinan, Sajeev John, and Ovidiu Toader, Phys. Rev. Lett. **90**, 123901 (2003).
[26] Sajeev John, Phys. Rev. Lett. **53**, 2169 (1984).
[27] Sajeev John, Phys. Today **44** (5), 32 (1991).
[28] V. P. Bykov, Sov. J. Quantum Electron. **4**, 861 (1975).
[29] Sajeev John and Jian Wang, Phys. Rev. Lett. **64**, 2418 (1990).
[30] Sajeev John and Marian Florescu, J. Opt. A, Pure Appl. Opt. **3**, S103 (2001).
[31] K. M. Ho, C. T. Chan, and C. M. Soukoulis, Phys. Rev. Lett. **65**, 3152 (1990).
[32] C. T. Chan, K. M. Ho, C. M. Soukoulis, R. Biswas, and M. Sigalas, Solid State Commun. **89**, 413 (1994).
[33] S. H. Sözüer, and P. J. Dowling, J. Mod. Opt. **41**, 231 (1994).
[34] E. Özbay, E. Michel, G. Tuttle, R. Biswas, M. Sigalas, and K.-M. Ho, Appl. Phys. Lett. **64**, 2059 (1994).
[35] S. Y. Lin, J. G. Fleming, D. L. Hetherington, B. K. Smith, R. Biswas, K. M. Ho, M. M. Sigalas, W. Zubrzycki, S. R. Kurtz, and Jim Bur, Nature (London) **394**, 251 (1998).
[36] Susumu Noda, Katsuhiro Tomoda, Noritsugu Yamamoto, and Alongkarn Chutinan, Science **289**, 604 (2000).
[37] Ovidiu Toader and Sajeev John, Science **292**, 1133 (2001).
[38] Ovidiu Toader and Sajeev John, Phys. Rev. E **66**, 016610 (2002).
[39] Kevin Robbie Maichael J. Brett, and Akhlesh Lakhtakia, J. Vac. Sci. Technol. A **13**, 2991 (1995).
[40] K. Robbie, M. J. Brett, and A. Lakhtakia, Nature (London) **384**, 616 (1996).

[41] Scott R. Kennedy, Michael J. Brett, Ovidiu Toader, and Sajeev John, Nano Lett. **2**, 59 (2002).
[42] Alvaro Blanco *et al.*, Nature (London) **405**, 437 (2000).
[43] Hernan Miguez *et al.*, Adv. Mater. (Weinheim, Ger.) **13**, 1634 (2001).
[44] E. Yablonovitch, T. J. Gmitter, and K. M. Leung, Phys. Rev. Lett. **67**, 2295 (1991).
[45] M. Christophersen, J. Carstensen, A. Feuerhake, and H. Föll, Mater. Sci. Eng., B **69**, 194 (2000).
[46] Timothy Y. M. Chan and Sajeev John, Phys. Rev. E **68**, 046607 (2003).
[47] M. Campbell, D. N. Sharp, M. T. Harrison, R. G. Denning, and A. J. Turberfield, Nature (London) **404**, 53 (2000).
[48] Ovidiu Toader, Timothy Y. M. Chan., and Sajeev John, Phys. Rev. Lett. **92**, 043905 (2004).
[49] R. Hillebrand, St. Senz, W. Hergert, and U. Gösele, J. Appl. Phys. **94**, 2758 (2003).
[50] R. Hillebrand and W. Hergert, Photonics Nanostruct. Fundam. Appl. **2**, 33 (2004).
[51] M. Deubel, M. Wegener, A. Kaso, and S. John (unpublished).
[52] Hernán Míguez, Nicolas Tétreault, Benjamin Hatton, San Ming Yang, Doug Perovic, and Geoffrey A. Ozin, Chem. Commun. (Cambridge) **2002**, 2736.